Regular Article

Yeast-template synthesized Fe-doped cerium oxide hollow microspheres for visible photodegradation of acid orange 7

CrossMark

Baoqin Zhao [a], Qian Shao [a,*], Luhan Hao [b], Li Zhang [c,*], Zhen Liu [d], Bing Zhang [a], Shengsong Ge [a], Zhanhu Guo [b,*]

[a] College of Chemical and Environmental Engineering, Shandong University of Science and Technology, Qingdao 266590, PR China
[b] Integrated Composites Laboratory (ICL), Department of Chemical & Biomolecular Engineering, University of Tennessee, Knoxville, TN 37996, USA
[c] School of Environmental and Materials Engineering, Shanghai Second Polytechnic University, Shanghai 201209, PR China
[d] Department of Physics and Engineering, Frostburg State University, Frostburg, MD, USA

GRAPHICAL ABSTRACT

Fe-doped cerium oxide hollow microspheres obtained using yeast as a bio-template have demonstrated higher photocatalytic activity in degrading acid orange 7 under visible irradiation.
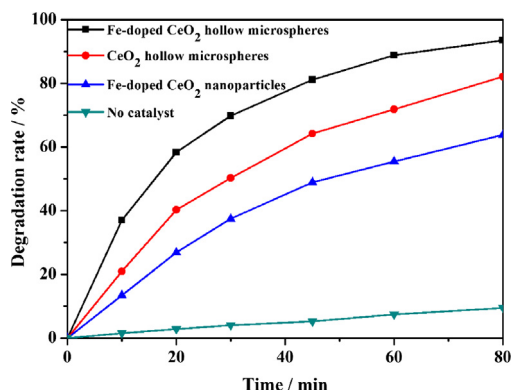
ARTICLE INFO

ABSTRACT

Fe-doped cerium oxide (CeO₂) hollow microspheres were successfully synthesized by a simple co-precipitation route using yeast as a bio-template and nitrate as the oxide precursor. The products were characterized by scanning electron microscopy, X-ray diffraction, X-ray photoelectron spectroscopy, N₂ adsorption–desorption isotherms and UV–Vis diffuse reflectance spectroscopy. It was found that the products had a well-defined ellipsoidal morphology and the size of the hollow microspheres was about 1.5–2.5 μm. The formation mechanism of Fe-doped CeO₂ hollow microspheres was proposed and discussed as well. The photocatalytic test results showed that the Fe-doped CeO₂ hollow microspheres exhibited a higher photocatalytic activity in the degradation of acid orange 7 (AO7) aqueous solutions containing H₂O₂ under visible irradiation compared with CeO₂ hollow microspheres and Fe-doped CeO₂ nanoparticles, which was attributed to their more oxygen vacancies, higher specific surface area

* Corresponding authors.
  E-mail addresses: shaoqian01@126.com (Q. Shao), zhangli@sspu.edu.cn (L. Zhang), zguo10@utk.edu (Z. Guo).

and lower band gap. The degradation rate of the Fe-doped CeO_2 hollow microspheres was found to be 93% after 80 min and the degradation reaction followed pseudo-first-order kinetics.

1. Introduction

Doped cerium oxides have been intensively studied over the past years because of their high thermal stability, oxygen storage capacity and catalytic activity. The properties of doped cerium oxides are closely related to their defect chemistry [1,2], which is mainly determined by the size, charge and concentration of the dopant cations. Doped cerium oxides have been reported for many applications such as photocatalysis [3,4], fuel cell [5,6], CO preferential oxidation [7,8], water gas shift reaction [9,10], partial oxidation of methane [11,12], and many others. Zr, Fe, Cu, Zn and Eu have been widely used as elements to dope ceria [13–17]. Among these, Fe can greatly increase the oxygen interchange capacity compared with other metal elements, because of the synergistic fenton and other reactions between the redox couple of the cerium (Ce^{4+}/Ce^{3+}) and iron (Fe^{3+}/Fe^{2+}) cations. Therefore, Fe-doped ceria system has received intense research interests in recent years.

Dyes are one of the major pollutants for water pollution [18–21], efficient dyes elimination is thus of great significance. Previous works demonstrated that Fe-doped ceria is an active photocatalyst for dyes degradation. For example, Pradhan et al. [22] synthesized iron-cerium mixed oxides by co-precipitation method and evaluated the solar light driven photocatalytic activity towards methylene blue, Congo red and phenol degradation. The results showed that 50% Fe-doping cerium oxides gave the highest degradation rate for all the tested dyes. Wandong et al. [14] prepared Fe-doped ceria materials of different doping amounts by hydrothermal method and demonstrated that the low doping amount of Fe^{3+} could effectively improve the concentration of Ce^{3+} and enhanced the degradation ability of AO7. Channei et al. [23] synthesized Fe-doped CeO_2 film by homogeneous precipitation and impregnation methods and evidenced that the optimal photocatalytic degradation of methyl orange under visible irradiation was achieved by 1.50 mol% Fe-doped CeO_2 film.

Fe-doped ceria materials have been synthesized by various techniques, including hydrothermal processes [3,24,25], co-precipitation [26–28], template method [29–31] and sol gel technique [32,33]. Among these, the template method has obvious advantages, such as easy control of morphology and facile synthesis conditions. However, the template synthesis of Fe-doped ceria materials has been rarely reported in previous studies. The yeast-templating method provides an economic, green, and convenient strategy compared with the traditional template-directed method. The cell wall of yeast primarily consists of glucan and mannan, which are rich in reactive functional groups, such as acid amides, hydroxyls and carbonyls [34–36], enabling the stabilization of the produced nanoparticles [37–40]. Currently, ZrO_2, Fe_2O_3, CeO_2, Co_3O_4 and SnO_2 [41–45] have been successfully synthesized using yeast templates, but Fe-doped CeO_2 hollow microspheres as photocatalyst prepared by yeast-templating method have not been reported.

In this work, Fe-doped CeO_2 hollow microspheres with high specific surface area and good thermal stability were prepared by a simple co-precipitation route using yeast as a bio-template. The photocatalytic performance was tested by measuring the decompositions of the AO7 aqueous solutions containing H_2O_2 under visible irradiation. Compared with CeO_2 hollow microspheres and Fe-doped CeO_2 nanoparticles, the Fe-doped CeO_2 hollow microspheres exhibit a higher photocatalytic degradation rate in degrading dye stuff under visible irradiation. The enhancement mechanism was proposed as well.

2. Experimental

2.1. Materials

Yeast powders were provided by Angel yeast Co. Ltd. $Ce(NO_3)_3 \cdot 6H_2O$, $Fe(NO_3)_3 \cdot 9H_2O$, NaOH, C_2H_6O and H_2O_2 (30%) were obtained from Kermel reagent Co. Ltd. (Tianjin China). AO7 was purchased from Shanghai Chemical Reagent Co. Ltd. (Shanghai, China). All the reagents were of analytical grade and used without any further purification. Distilled water was used throughout the experiments.

2.2. Synthesis of Fe-doped CeO_2 hollow microspheres

In a typical process, 1.0 g yeast powders were washed with absolute ethanol and distilled water for three times. The washed yeast was dispersed into 20 mL distilled water and was mechanically stirred thoroughly at ambient temperature. 20 mL mixed salt solution (1.0 g $Ce(NO_3)_3 \cdot 6H_2O$ and 0.01 g $Fe(NO_3)_3 \cdot 9H_2O$) was added to the above solution under stirring and kept stirring for one hour. Then, a solution (0.2 g NaOH in 10 mL distilled water) was added dropwise to the mixture under further stirring for 1 h. The mixture was aged at ambient temperature for 12 h. The precipitate was collected by centrifugation, and washed twice with distilled water and once with ethanol. Then, the precipitate was dried at 80 °C for 6 h. Finally, the Fe-doped CeO_2 hollow microspheres were obtained by calcining from room temperature to 600 °C with a heating rate of 1 °C min^{-1} and maintaining at 600 °C for 2 h. Similarly, CeO_2 hollow microspheres, and Fe-doped CeO_2 nanoparticles without templates were prepared by the same method for the comparison of photocatalytic performance.

2.3. Characterization

The morphologies and elemental analysis of the prepared products were examined by a scanning electron microscopy (SEM, SU-70, Hitachi, Japan) fitted with an energy dispersive spectrometer (EDS) at an acceleration voltage of 30 kV. The crystal structures of the samples were analyzed by X-ray diffraction (XRD, ultima IV, Rigaku, Japan) with Cu Kα radiation (λ = 0.15418 nm) at a scanning rate of 8°/min in 2θ range from 20° to 80°. X-ray photoelectron spectroscopy (XPS) measurements were determined with an X-ray spectrometer Kα (Thermo Scientific, USA). The specific surface area of the samples was measured using a surface area analyzer (BET, Tristar II 3020, Micromeritics, America) at liquid nitrogen temperature (77 K) after the products were vacuum treated at 120 °C for 5 h. The UV–Vis diffuse reflectance spectra of the products were recorded on a UV–2550 UV–Vis spectrophotometer (UV–Vis DRS, UH4150, Hitachi, Japan).

2.4. Photocatalytic activity test

The photocatalytic activity was evaluated by measuring the decomposition of the AO7 aqueous solutions containing H_2O_2 under visible irradiation. In a typical visible irradiation degradation experiment, 20 mg catalyst powders were dispersed in 50 mL AO7

aqueous solution (20 mg·L^{-1}). The suspensions were magnetically stirred in dark for 1 h to reach adsorption equilibrium, then H_2O_2 solution was added to reach a concentration of 1 mmol·L^{-1}, the mixture was transferred to the photochemical reactor under irradiation of sun-light (Xe lamp, 14 V, 15 A, 320~1100 nm). At certain time intervals, 2 mL solution was taken out and immediately centrifuged. The AO7 supernatant absorbance was measured by UH-4150 UV–visible adsorption spectrophotometer (wavelength is 484 nm).

3. Results and discussion

3.1. SEM and EDS analysis

Fig. 1A shows the SEM image of Fe-doped CeO_2 nanoparticles after calcination, the sample is observed to be irregular and agglomerated. The SEM image of the primitive yeast cells, Fig. 1B, illustrates that the original yeast cells are approximately spherical or ellipsoid with the diameter ranging from 3.0 to 4.5 μm and have a good dispersity. The Fe-doped CeO_2 hollow microspheres before calcination (Fig. 1D) inherit the ellipsoidal morphology of primitive yeast cells, and an increasement in particle size (ca. 0.5 μm) is observed, indicating that the $Ce(OH)_3$ and $Fe(OH)_3$ particles were coated on the surface of the yeast cell walls. After calcination treatment, the obtained CeO_2 hollow microspheres (Fig. 1C) and Fe-doped CeO_2 hollow microspheres (Fig. 1E–H) still retain the morphology of yeast cells, but the size of the above two samples is reduced to ca. 1.5–2.5 μm. The shrinkage of the samples is attributed to the removal of yeasts during heat treatment. And the sample is not significantly damaged during the calcination process, indicating the good thermal stability of CeO_2 hollow microspheres and Fe-doped CeO_2 hollow microspheres. Fig. 1G exhibits a surface-concave Fe-doped CeO_2 microsphere, which demonstrates that the as-prepared Fe-doped CeO_2 particles are hollow spheres. The surfaces of as-synthesized Fe-doped CeO_2 microspheres (Fig. 1H) are observed to be constructed by many nanoparticles. EDS spectra of Fe-doped CeO_2 hollow microspheres after calcination (Fig. 1I) evidence the presence of Fe, Ce, C, O and Pt elements. Fe and Ce derived from the Fe-doped CeO_2 hollow microspheres; C resulted from the yeast cell; O was partly from the Fe-doped CeO_2 hollow microspheres and partly from the yeast cell; Pt was assumed to derive from the metal spraying process before SEM studies. No other elements were detected, indicating that Fe-doped CeO_2 hollow microspheres were free of impurity.

3.2. XRD analysis

Fig. 2A shows the XRD patterns of Fe-doped CeO_2 nanoparticles (a), CeO_2 hollow microspheres (b), and Fe-doped CeO_2 hollow microspheres (c). The XRD patterns show that all diffraction peaks of the as-prepared samples matched well with the powder diffraction data for CeO_2 (JCPDS card No. 34-0394), no extra XRD peaks arising from the iron oxide or other impurities are observed. The broadness of the diffraction peaks relates to a decrease in the crystallite size, the crystallite size of as-prepared samples is estimated by Scherrer formula (1) [46]:

$$D = 0.89\lambda/\beta\cos\theta \tag{1}$$

where λ is the X-ray wavelength, 1.5418 Å (Cu Kα), β is X-ray half-width height (FWHM) and θ is the diffraction angle. The mean crystallite size of Fe-doped CeO_2 hollow microspheres estimated by Scherrer formula from its XRD patterns is ~8 nm (D_{111}), whereas those of Fe-doped CeO_2 nanoparticles and CeO_2 hollow microspheres are ~14 and ~9 nm, respectively. This further indicates that the obtained microspheres are made of many nanoparticle building

blocks. Thus, the diffraction peaks of Fe-doped CeO_2 hollow microspheres are looked relatively wider. In addition, it is noted that the CeO_2 characteristic peaks in the Fe-doped CeO_2 hollow microspheres shift to higher 2θ positions (see the enlarged section in Fig. 2B). This phenomenon is associated with the variations in lattice parameters [47,48]. In order to better understand, the mean parameter of the ceria lattice has been calculated on the basis of the XRD peak of crystal plane. The lattice parameter of the Fe-doped CeO_2 hollow microspheres (0.5396 nm) is a little smaller than that of the Fe-doped CeO_2 nanoparticles (0.5404 nm) and CeO_2 hollow microspheres (0.5410 nm). It indicates that Fe^{3+} cations have been successfully incorporated into the ceria lattice and result in a contraction of the cell parameter, which in turn leads to the occurrence of this phenomenon in Fig. 2B.

3.3. XPS analysis

Fig. 3 shows the Ce 3d (Fig.3A), O 1s (Fig. 3B), and Fe 2p (Fig. 3C) spectra of the Fe-doped CeO_2 nanoparticles, CeO_2 hollow microspheres and Fe-doped CeO_2 hollow microspheres. In the Ce 3d spectra, the peaks labeled v and u refer to the $3d_{5/2}$ and $3d_{3/2}$ spin orbit components, respectively. The peaks labeled v, v'', v''', u, u'', u''' can be assigned to Ce^{4+} and v', u' to Ce^{3+} [49]. The relative concentration of Ce^{3+} and Ce^{4+} can be obtained by calculating the integrated areas under the curve of each deconvoluted peaks [50], and the result is summarized in Table 1. As given in Table 1, the Fe-doped CeO_2 hollow microspheres show a relatively higher proportion of Ce^{3+}. In the O 1s spectra, there are two main peaks labeled O_I and O_{II}. Generally, the former represents bulk oxygen (O^{2-}), while the latter corresponds to various surface oxygen species (O_2^{2-}), which are known to be related to the activity of oxidization [51,52]. The calculated relative concentration of oxygen species is also shown in Table 1. Compared with the Fe-doped CeO_2 nanoparticles and CeO_2 hollow microspheres, the relative concentration of O_2^{2-} is higher in Fe-doped CeO_2 hollow microspheres. This result is consistent with the concentration of Ce^{3+}. The main reason is that when Fe^{3+} ions are incorporated within CeO_2, the introduced Ce^{3+} and oxygen vacancies are necessary to increase for charge compensation [53]. In the Fe 2p spectra, no obvious peaks of Fe 2p can be observed, indicative of low Fe^{3+} content.

Two mechanisms have been proposed about the concentration of oxygen vacancies for the metal ion doping in the CeO_2, the vacancy compensation [14] and interstitial compensation mechanism [54]. For the small Fe^{3+} doping amount, the vacancy compensation mechanism [14] is the dominant factor to change the concentration of oxygen vacancy. Therefore, the increased concentration of oxygen vacancies in this paper should be attributed to the vacancy compensation mechanism [14]. As shown in Fig. 4, besides the own inherent oxygen vacancy in the CeO_2 (mode 1), there are two additional kinds of oxygen vacancies: (i) one Ce^{4+} cation is replaced by an Fe^{3+} cation, which reduces the adjacent Ce^{4+} cations to Ce^{3+} cations, resulting in the formation of the oxygen vacancy (mode 2). (ii) one oxygen vacancy (mode 3) is established to balance the charge when two adjacent Ce^{4+} cations are replaced by two Fe^{3+} cations. It can be seen from Fig. 4 that when low-content Fe^{3+} are doped into the CeO_2 lattice, the concentration of oxygen vacancies and Ce^{3+} cations will increase together.

3.4. BET surface area analysis

Fig. 5 presents the nitrogen adsorption-desorption isotherms of Fe-doped CeO_2 nanoparticles (Fig. 5A), CeO_2 hollow microspheres (Fig. 5B) and Fe-doped CeO_2 hollow microspheres (Fig. 5C). According to the IUPAC classification, the isotherms of samples can be classified as a type IV isotherm, which is a typical characteristic of the mesoporous materials [43]. The BET specific surface area
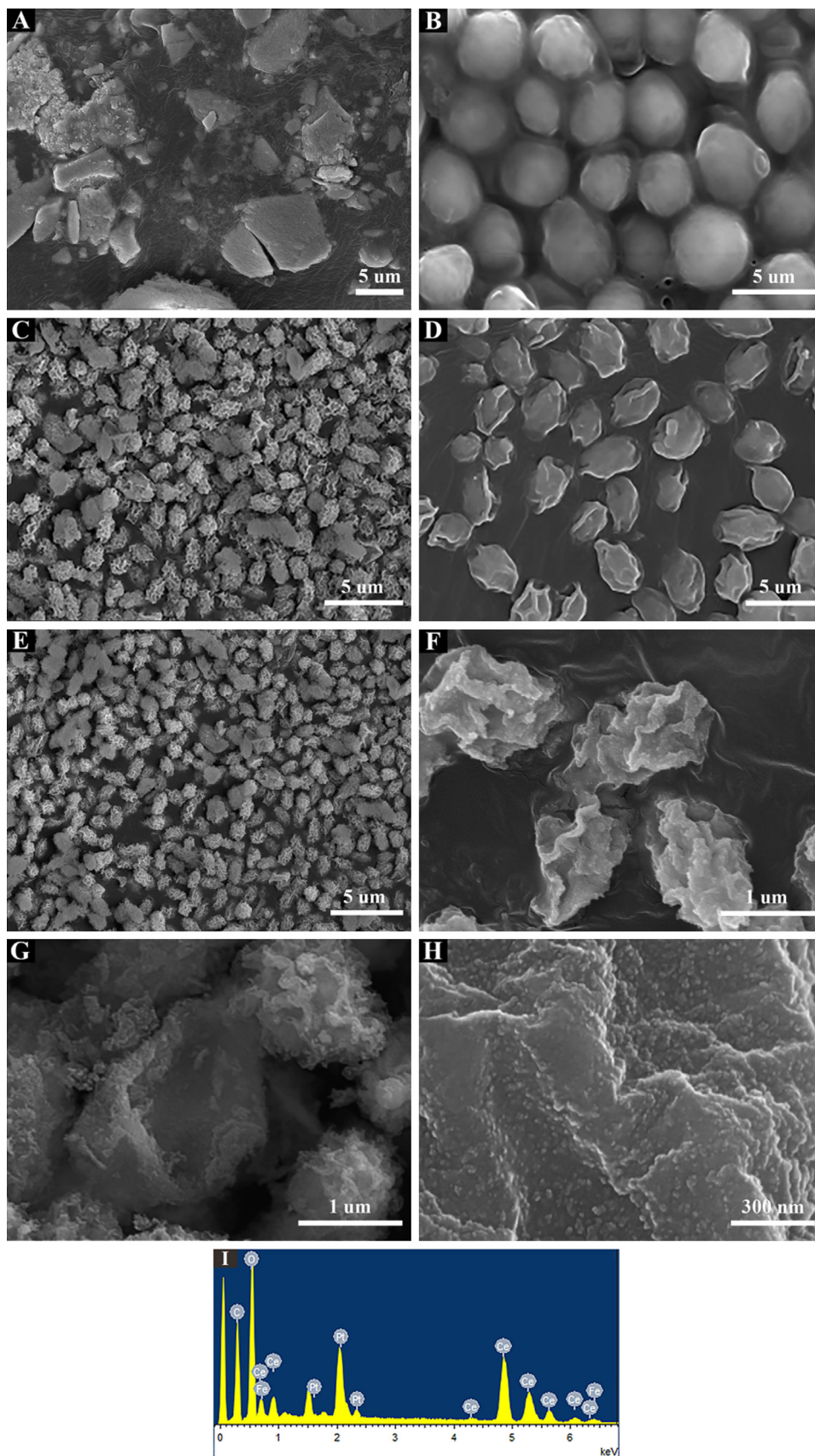
Fig. 1. SEM images of Fe-doped CeO$_2$ nanoparticles (A), yeast template (B), CeO$_2$ hollow microspheres (C), Fe-doped CeO$_2$ hollow microspheres before (D) and after (E, F, G, H) calcination, EDS spectra of Fe-doped CeO$_2$ hollow microspheres (I).
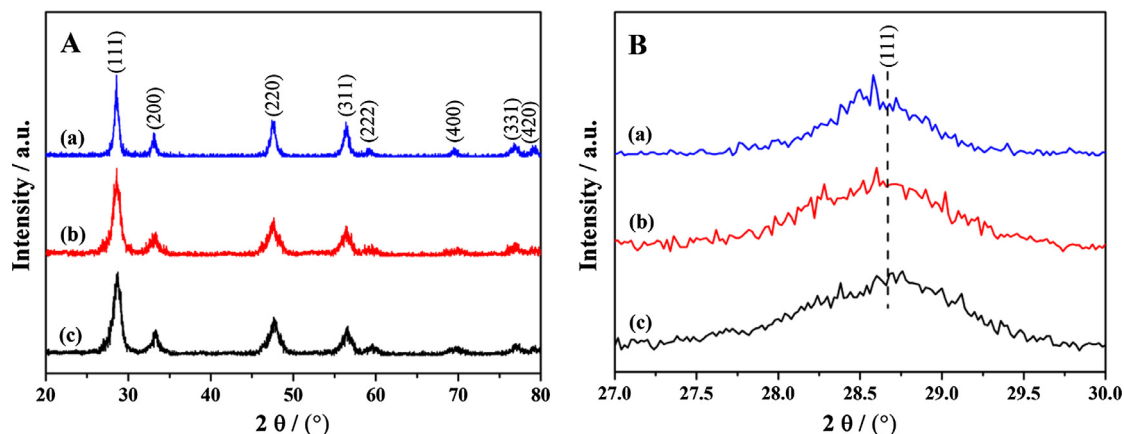
Fig. 2. XRD patterns (A, B) of Fe-doped CeO$_2$ nanoparticles (a), CeO$_2$ hollow microspheres (b) and Fe-doped CeO$_2$ hollow microspheres (c).
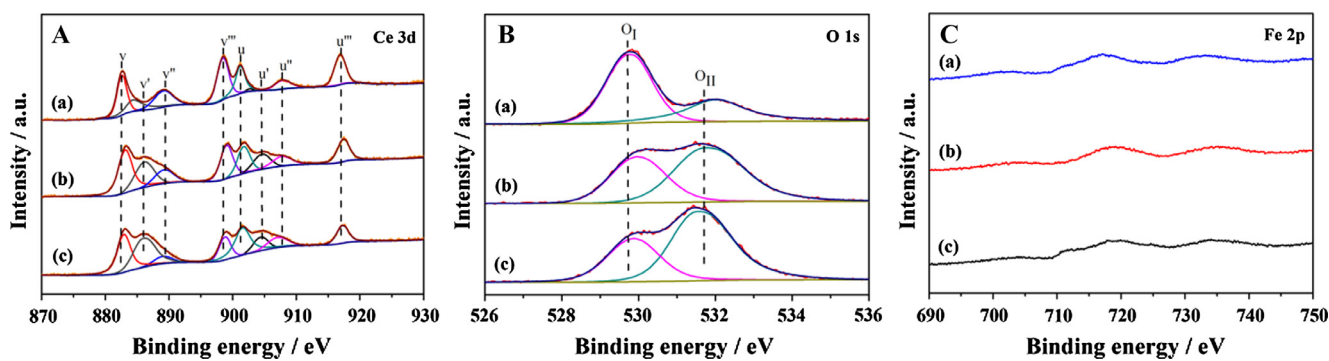

Fig. 3. XPS spectra of Ce 3d (A), O 1s (B), and Fe 2p (C) of different samples: Fe-doped CeO$_2$ nanoparticles (a), CeO$_2$ hollow microspheres (b) and Fe-doped CeO$_2$ hollow microspheres (c).

Table 1
Surface compositions and oxidation states of O and Ce species by XPS analysis.

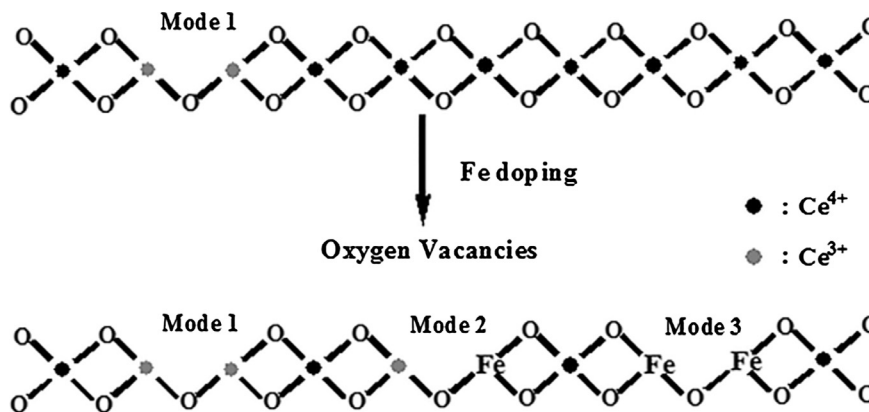| Samples	O species/%		Ce species/%	
	O$_2^{2-}$	O^{2-}	Ce^{3+}	Ce^{4+}
Fe-doped CeO$_2$ nanoparticles	27.12	72.88	9.04	90.96
CeO$_2$ hollow microspheres	58.72	41.28	23.11	76.89
Fe-doped CeO$_2$ hollow microspheres	73.93	26.07	31.03	68.97

Fig. 4. Different kinds of oxygen vacancies in Fe-doped CeO$_2$ hollow microspheres.

of the Fe-doped CeO$_2$ hollow microspheres is 43.49 m^2/g, which is much higher than that of the Fe-doped CeO$_2$ nanoparticles (25.08 m^2/g) and CeO$_2$ hollow microspheres (30.55 m^2/g). The main reasons are that: (1) the use of yeast template enables a hollow structure, leading to an increased specific surface area; (2) the substitution of Ce cations with smaller Fe cations results in a
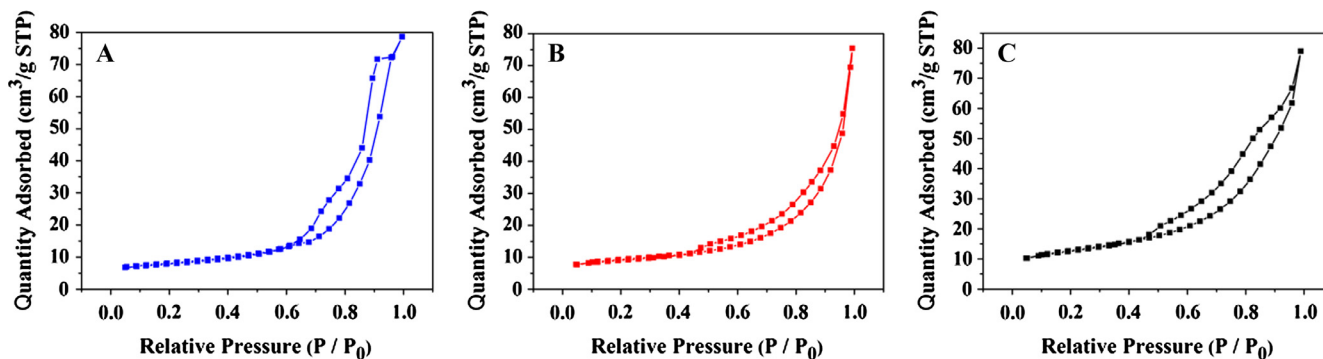
Fig. 5. Nitrogen adsorption-desorption isotherms of Fe-doped CeO_2 nanoparticles (A), CeO_2 hollow microspheres (B) and Fe-doped CeO_2 hollow microspheres (C).

decrease of particle size, thereby increasing the specific surface area of the sample.

3.5. UV–Vis diffuse reflectance spectra analysis

Fig. 6A shows the UV–Vis absorption spectra of the as-prepared samples. As can be seen from Fig. 6A, compared with Fe-doped CeO_2 nanoparticles and CeO_2 hollow microspheres, the UV–Vis spectra of Fe-doped CeO_2 hollow microspheres show distinctly higher absorptions in the UV and visible regions. Using absorption spectrum data, the band gap of the prepared samples can be estimated using Eq. (2) [3]:

$$(Ah\nu)^2 = K(h\nu - E_g) \qquad (2)$$

where A is the absorption coefficient, $h\nu$ is the photon energy, E_g is the band gap energy for direct transitions, and K is a proportionality constant. The normalized graphs of $(Ah\nu)^2$ for the photon energy of the as-prepared samples are shown in Fig. 6B. The band gap energy of Fe-doped CeO_2 hollow microspheres is about 3.10 eV. Compared with the Fe-doped CeO_2 nanoparticles (E_g = 3.37 eV) and CeO_2 hollow microspheres (E_g = 3.21 eV), the decrease in the band gap energy of Fe-doped CeO_2 hollow microspheres may be attributed to the formation of impurity energy level caused by Fe-doping or defects created by yeasts and Fe ions, which is also observed in other studies [43,55]. The intrinsic band gap favors an easier excitation under visible light region, leading to an enhanced photocatalytic performance.

3.6. Formation mechanism

The mechanism for the formation of Fe-doped CeO_2 hollow microspheres is proposed in Fig. 7. The whole process can be described as follows: (i) The yeast is a single-cell eukaryotic microorganism with a high rate of reproduction, the wall of the living cell of yeasts can prevent inorganic salt or ions from entering the interior of the cells. (ii) There are many reactive functional groups on the cell wall of yeast, such as acid amides, hydroxyls and carbonyls [34–36]. Therefore, Ce^{3+} cation and Fe^{3+} cation can be absorbed onto the cell wall through coordination or electrostatic attractions. These groups not only have interaction with crystal element but also guide nucleation, growth and crystallization of Fe-doped CeO_2 crystals. (iii) $Ce(OH)_3$ and $Fe(OH)_3$ were formed on the cell walls of yeast after adding NaOH. After that, the sample was dried at 80 °C. At this time, the yeast cell was dead. Then, free water was evaporated and the hydration water in the inner cell was also escaped. Other compositions (such as cell nucleus, mitochondria, etc.) are attached to the inner wall of the yeast to keep the original shape of the yeast. (iv) Finally, after calcination at 600 °C, the organic matters in the yeast were removed, and $Ce(OH)_3$, $Fe(OH)_3$@yeast microspheres were converted to Fe-doped CeO_2 hollow microspheres.

3.7. Photocatalytic activity

Fig. 8 shows the photocatalytic activity of Fe-doped CeO_2 hollow microspheres toward the degradation of AO7 with the presence of various concentrations of H_2O_2. As observed, the highest
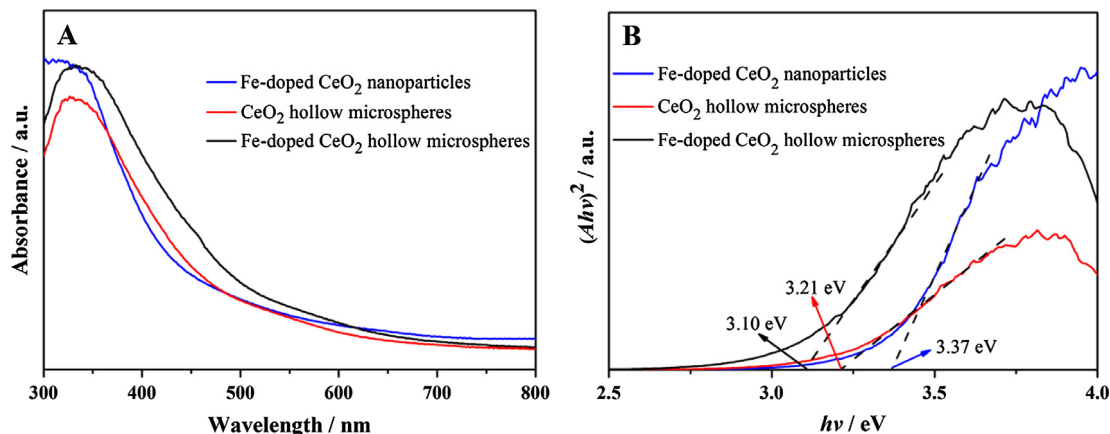

Fig. 6. UV–vis adsorption spectra (A) of Fe-doped CeO_2 nanoparticles, CeO_2 hollow microspheres and Fe-doped CeO_2 hollow microspheres, and the plotting of $(Ah\nu)^2$ vs. $h\nu$ based on the direct transition (B).
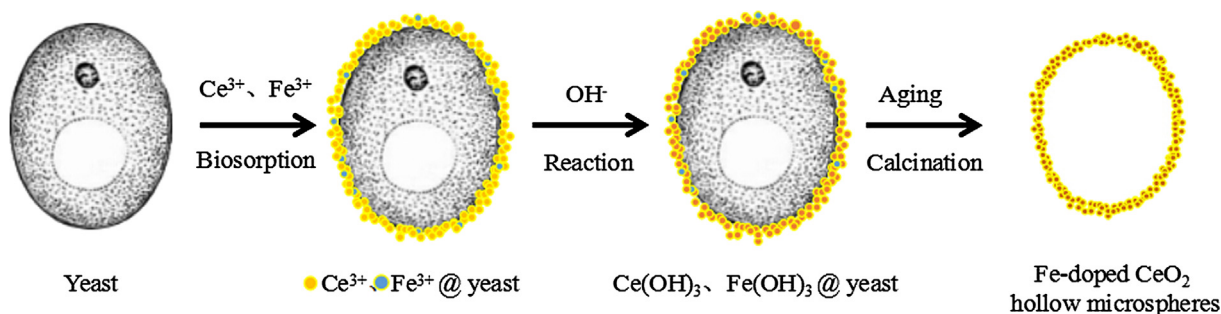
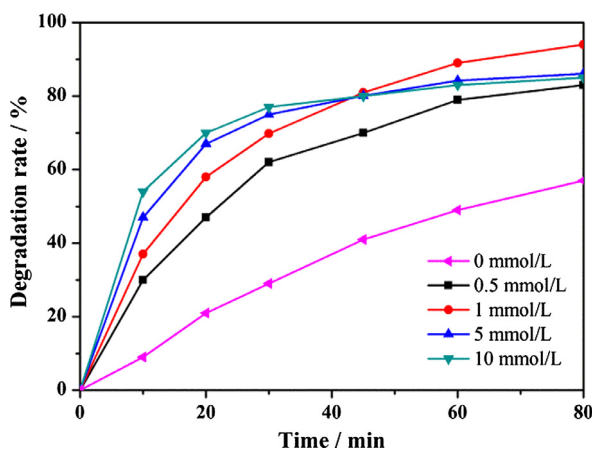**Fig. 7.** Schematic illustration of proposed formation mechanism of Fe-doped CeO$_2$ hollow microspheres.

Fig. 8. Degradation efficiency of AO7 aqueous solution under different concentrations of H$_2$O$_2$.

degradation rate is achieved at a H$_2$O$_2$ concentration of 1 mmol·L^{-1}, while 0 mmol·L^{-1} H$_2$O$_2$ gives the minimum degradation rate of AO7. On the other hand, the degradation of AO7 is relatively quicker in the initial phase but then significantly slows down and even stops (see that with 5 mmol·L^{-1} and 10 mmol·L^{-1}

H$_2$O$_2$) with a higher concentration of H$_2$O$_2$, this phenomenon is explained in conjunction with Fig. 9. As shown in Fig. 9, after dark reaction, the adsorption-desorption equilibrium of AO7 is established on the surface of CeO$_2$. The subsequent addition of H$_2$O$_2$ induces a competitive adsorption between AO7 and H$_2$O$_2$, which induces partial desorption and a simultaneous degradation of adsorbed AO7. H$_2$O$_2$ with a higher concentration results in a quicker desorption as well as a larger degradation for AO7. However, as the reaction progresses, it also leads to over-complexation between CeO$_2$ and H$_2$O$_2$, which hinders further degradation of AO7 [56].

The photocatalytic activity tests were therefore conducted in AO7 aqueous solutions containing 1 mmol·L^{-1} H$_2$O$_2$ under visible irradiation. And the time-dependent UV–Vis absorption spectra of AO7 with the use of different catalysts are shown in Fig. 10A–D. The degradation rate of the AO7 aqueous solutions containing H$_2$O$_2$ was more than 93% under visible irradiation in 80 min using the Fe-doped CeO$_2$ hollow microspheres as photocatalysts (Fig. 10D). The digital photo (Fig. 10D, inset) shows that after 80 min, AO7 aqueous solution was entirely decolorized, suggesting the excellent photocatalytic activity of Fe-doped CeO$_2$ hollow microspheres. In sharp contrast, AO7 degradation rate of only 64%, 81% and 9% was observed for degradation reaction catalyzed by Fe-doped CeO$_2$ nanoparticles, CeO$_2$ hollow microspheres as photocatalyst and without photocatalyst under the same experimental conditions, respectively, as shown in Fig. 10E.
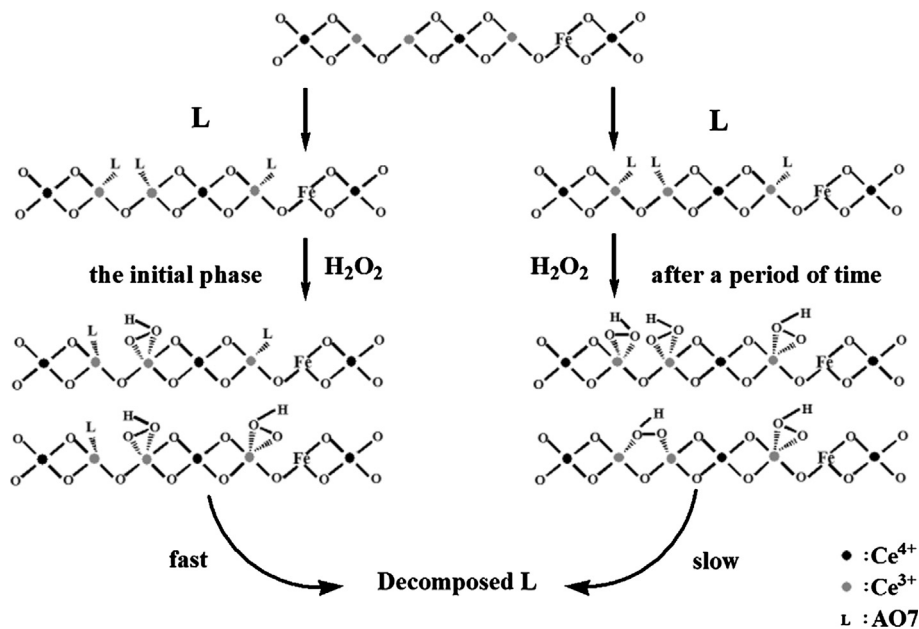

Fig. 9. Catalytic oxidation mechanism in the Fe/CeO$_2$/H$_2$O$_2$ system.
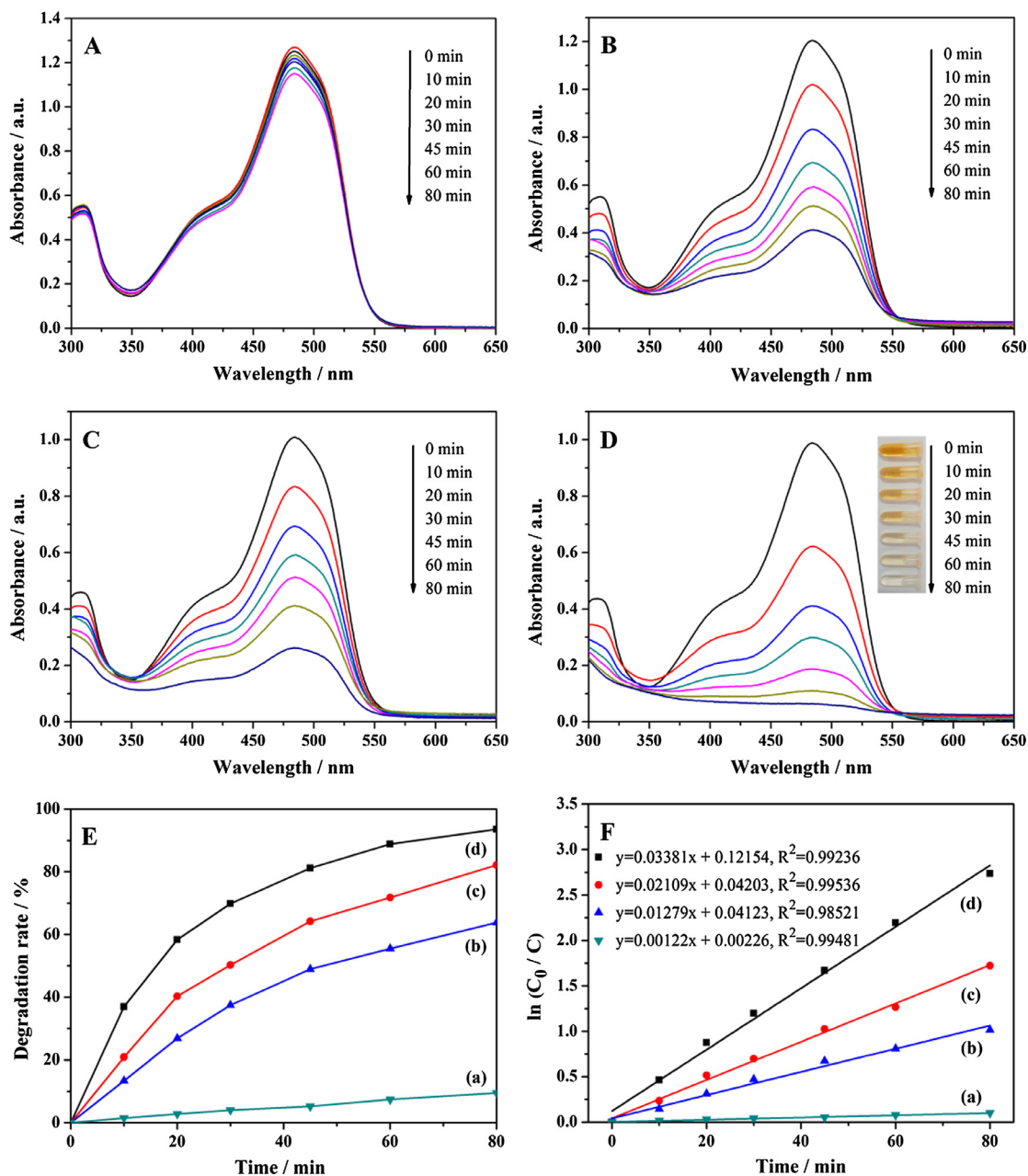
Fig. 10. Photocatalytic degradation of the AO7 aqueous solutions containing H_2O_2 under different conditions: AO7 blank (A), adding Fe-doped CeO_2 nanoparticles (B), adding CeO_2 hollow microspheres (C), adding Fe-doped CeO_2 hollow microspheres (D); the degradation efficiency at different irradiation times (E) and the photodegradation kinetic curves(F): AO7 (a), Fe-doped CeO_2 nanoparticles (b), CeO_2 hollow microspheres (c) and Fe-doped CeO_2 hollow microspheres (d).

In order to better understand the photocatalytic efficiency of the as-prepared samples, the photocatalytic degradation kinetics of AO7 was also investigated. The photocatalytic degradation process fits well with pseudo-first-order kinetics as shown in Eq. (3) [57]:

$$\ln(C_0/C) = kt \tag{3}$$

where k is the first-order apparent rate constant and t is the light irradiation time. The value of apparent rate constant k calculated from corresponding slope of the pseudo-first-order linear simulation curve is shown in the Fig. 10F. It is observed that the k value of Fe-doped CeO_2 hollow microspheres ($0.03381 \, \text{min}^{-1}$) is much larger than that of Fe-doped CeO_2 nanoparticles ($0.01279 \, \text{min}^{-1}$), CeO_2 hollow microspheres ($0.02109 \, \text{min}^{-1}$) and the self-degradation of the AO7 aqueous solutions containing H_2O_2 ($0.00122 \, \text{min}^{-1}$). Compared with CeO_2 hollow microspheres and

Fe-doped CeO_2 nanoparticles, Fe-doped CeO_2 hollow microspheres exhibit a higher photocatalytic degradation rate in degrading AO7 aqueous solutions containing H_2O_2 under visible irradiation due to their more oxygen vacancies, higher specific surface area and lower band gap. As the Fe-doped CeO_2 hollow microspheres display a larger specific surface area (BET analysis) and more oxygen vacancies (XPS analysis), it possesses more active sites on the surface for binding of substrate, which can effectively enhance the photocatalytic activity of the catalyst.

4. Conclusion

In summary, Fe-doped CeO_2 hollow microspheres were successfully synthesized by a simple co-precipitation route using yeast as a bio-template and nitrate as the oxide precursor. This was the first

report on the use of bio-templates to synthesize Fe-doped ceria materials. Compared with previous studies, the presented preparation method was simple and the product morphology was controllable. The as-prepared Fe-doped CeO_2 hollow microspheres had a well-defined ellipsoidal morphology and uniform diameters of 1.5–2.5 μm. The possible formation mechanism of Fe-doped CeO_2 hollow microspheres involved the interaction between Ce^{3+}, Fe^{3+}- and the inherent functional groups on the cell walls of yeast. Compared to CeO_2 hollow microspheres and Fe-doped CeO_2 nanoparticles, Fe-doped CeO_2 hollow microspheres exhibited a higher photocatalytic performance in degrading AO7 aqueous solutions containing H_2O_2 under visible irradiation due to their more oxygen vacancies, higher specific surface area and lower band gap. The degradation rate of the Fe-doped CeO_2 hollow microspheres was found to be 93% after 80 min and the degradation reaction followed pseudo-first-order kinetics. In addition, this bio-template strategy could be generally extended to the preparation of other composite oxide hollow microspheres.

References

[1] W. Yu, J. Zhu, L. Qi, C. Sun, F. Gao, L. Dong, Y. Chen, J. Colloid Interface Sci. 364 (2011) 435–442.
[2] B. Chen, Z. Zhu, Y. Guo, Y. Qiu, J. Zhao, J. Colloid Interface Sci. 398 (2013) 142–151.
[3] M. Radović, Z. Dohčević-Mitrović, A. Golubović, V. Fruth, S. Preda, M. Šćepanović, Z.V. Popović, Ceram. Int. 39 (2013) 4929–4936.
[4] N. Chubar, V. Gerda, D. Banerjee, G. Yablokova, J. Colloid Interface Sci. 487 (2016) 388–400.
[5] J. Marrero-Jerez, S. Larrondo, E. Rodríguez-Castellón, P. Núñez, Ceram. Int. 40 (2014) 6807–6814.
[6] B. Liang, T. Suzuki, K. Hamamoto, T. Yamaguchi, H. Sumi, Y. Fujishiro, B.J. Ingram, J.D. Carter, J. Power Sources 202 (2012) 225–229.
[7] K. Sirichaiprasert, A. Luengnaruemitchai, S. Pongstabodee, Int. J. Hydrogen Energy 32 (2007) 915–926.
[8] Q. Yu, X. Wu, C. Tang, L. Qi, B. Liu, F. Gao, K. Sun, L. Dong, Y. Chen, J. Colloid Interface Sci. 354 (2011) 341–352.
[9] G.K. Reddy, P. Boolchand, P.G. Smirniotis, J. Catal. 282 (2011) 258–269.
[10] D.W. Jeong, H.S. Na, J.O. Shim, W.J. Jang, H.S. Roh, Catal. Sci. Technol. 5 (2015) 3706–3713.
[11] K. Li, H. Wang, Y. Wei, D. Yan, Chem. Eng. J. 173 (2011) 574–582.
[12] A. Hornés, M.J. Escudero, L. Daza, A. Martínez-Arias, J. Power Sources 249 (2014) 520–526.
[13] A. Morikawa, T. Suzuki, T. Kanazawa, K. Kikuta, A. Suda, H. Shinjo, Appl. Catal. B: Environ. 78 (2008) 210–221.
[14] W. Cai, F. Chen, X. Shen, L. Chen, J. Zhang, Appl. Catal. B: Environ. 101 (2010) 160–168.
[15] M. Piumetti, S. Bensaid, T. Andana, N. Russo, R. Pirone, D. Fino, Appl. Catal. B: Environ. 205 (2017) 455–468.
[16] O.H. Laguna, M.A. Centeno, F. Romero-Sarria, J.A. Odriozola, Catal. Today 172 (2011) 118–123.
[17] W.Y. Hernández, M.A. Centeno, F. Romerosarria, J.A. Odriozola, J. Phys. Chem. C. 113 (2009) 5629–5635.
[18] A. Omidvar, B. Jaleh, M. Nasrollahzadeh, J. Colloid Interface Sci. 496 (2017) 44–50.
[19] S. Muthulingam, I.H. Lee, P. Uthirakumar, J. Colloid Interface Sci. 455 (2015) 101–109.
[20] L. Zhang, W. Yu, C. Han, J. Guo, Q. Zhang, H. Xie, Q. Shao, Z. Sun, Z. Guo, J. Electrochem. Soc. 164 (2017) H651–H656.
[21] T. Liu, K. Yu, L. Gao, H. Chen, N. Wang, L. Hao, T. Li, H. He, Z. Guo, J. Mater. Chem. A. 5 (2017) 17848–17855.
[22] G.K. Pradhan, K.M. Parida, IJEST™ 2 (2010) 53–65.
[23] D. Channei, B. Inceesungvorn, N. Wetchakun, S. Ukritnukun, A. Nattestad, J. Chen, S. Phanichphant, Sci Rep 4 (2014) 5757.
[24] W. Wang, Q. Zhu, Q. Dai, X. Wang, Chem. Eng. J. 307 (2017) 1037–1046.
[25] H. Li, K. Li, H. Wang, X. Zhu, Y. Wei, D. Yan, X. Cheng, K. Zhai, Appl. Surf. Sci. 390 (2016) 513–525.
[26] F. Abbas, T. Jan, J. Iqbal, M.S.H. Naqvi, Curr. Appl. Phys. 15 (2015) 1428–1434.
[27] S. Mansingh, D.K. Padhi, K.M. Parida, Int. J. Hydrogen Energy 41 (2016) 14133–14146.
[28] K. Li, M. Haneda, P. Ning, H. Wang, M. Ozawa, Appl. Surf. Sci. 289 (2014) 378–383.
[29] M.O. Mazan, A.F. Craievich, E.B. Halac, M.C.A. Fantini, D.G. Lamas, S.A. Larrondo, Ceram. Int. 41 (2015) 13721–13730.
[30] H. Wang, Z. Qu, H. Xie, N. Maeda, L. Miao, Z. Wang, J. Catal. 338 (2016) 56–67.
[31] H. Lin, Z. Ma, L. Ding, J. Qiu, C. Liang, Chinese, J. Catal. 29 (2008) 418–420.
[32] S. Acharya, A. Bandyopadhyay, S. Modak, S. Mukherjee, D. Das, P.K. Chakrabarti, J. Magn. Magn. Mater. 321 (2009) 2701–2706.
[33] P.C.A. Brito, D.A.A. Santos, J.G.S. Duque, M.A. Macêdo, Physica B. 405 (2010) 1821–1825.
[34] B. Bo, P. Wang, W. Le, Y. Li, Z. Chen, Mater. Chem. Phys. 114 (2009) 26–29.
[35] Y. Ma, L. Lv, Y. Guo, Y. Fu, Q. Shao, T. Wu, S. Guo, K. Sun, X. Guo, E.K. Wujcik, Z. Guo, Polymer 128 (2017) 12–23.
[36] Y. Zheng, Y. Zheng, S. Yang, Z. Guo, T. Zhang, H. Song, Q. Shao, Green. Chem. Lett. Rev. 10 (2017) 202–209.
[37] Z. Sun, L. Zhang, F. Dang, Y. Liu, Z. Fei, Q. Shao, H. Lin, J. Guo, L. Xiang, N. Yerra, Z. Guo, Crystengcomm 19 (2017) 3288–3298.
[38] Y. Li, X. Wu, J. Song, J. Li, Q. Shao, N. Cao, N. Lu, Z. Guo, Polymer 124 (2017) 41–47.
[39] K. Sun, R. Fan, Y. Yin, J. Guo, X. Li, Y. Lei, L. An, C. Cheng, Z. Guo, J. Phys. Chem. C. 121 (2017) 7564–7571.
[40] K. Sun, P. Xie, Z. Wang, T. Su, Q. Shao, J. Ryu, X. Zhang, J. Guo, A. Shankar, J. Li, R. Fan, D. Cao, Z. Guo, Polymer 125 (2017) 50–57.
[41] X. Fan, X. Song, X. Yang, L. Hou, Mater. Res. Bull. 46 (2011) 1315–1319.
[42] P. Zheng, Z. Tong, B. Bai, J. Solid State Chem. 235 (2016) 119–124.
[43] G. Mu, Q. Wei, Y. Huang, J. Rare Earths. 33 (2015) 1329–1334.
[44] L. Yang, W. Guan, B. Bai, Q. Xu, Y. Xiang, J. Alloys Compd. 504 (2010) L10–L13.
[45] G. Xu, X. Zhang, H. Cui, Z. Zhang, J. Ding, J. Wu, Powder Technol. 301 (2016) 96–101.
[46] X. Zhou, T. Su, Y. Jiang, Z. Qin, H. Ji, Z. Guo, Chem. Eng. Sci. 153 (2016) 10–20.
[47] F. Lin, X. Wu, D. Weng, Catal. Today 175 (2011) 124–132.
[48] X. Zhang, J. Wei, H. Yang, X. Liu, W. Liu, C. Zhang, Y. Yang, Eur. J. Inorg. Chem. 2013 (2013) 4443–4449.
[49] H. Zhang, F. Gu, Q. Liu, J. Gao, L. Jia, T. Zhu, Y. Chen, Z. Zhong, F. Su, RSC Adv. 4 (2014) 14879.
[50] C. Korsvik, S. Patil, S. Seal, W.T. Self, Chem. Commun. 10 (2007) 1056.
[51] G. Zou, Y. Xu, S. Wang, M. Chen, W. Shangguan, Catal. Sci. Technol. 5 (2015) 1084–1092.
[52] X. Liu, H. Yang, L. Han, W. Liu, C. Zhang, X. Zhang, S. Wang, Y. Yang, Crystengcomm 15 (2013) 7769–7775.
[53] J.R. Vargas-Garcia, R. Tu, T. Goto, Thin Solid Films 520 (2012) 1851–1855.
[54] F.J. Pérezalonso, M.L. Granados, M. Ojeda, T. Herranz, S. Rojas, P. Terreros, J.L. Fierro, M. Gracia, J.R. Gancedo, J. Phys. Chem. B. 110 (2013) 23870.
[55] D. Channei, B. Inceesungvorn, N. Wetchakun, S. Phanichphant, A. Nakaruk, P. Koshy, C.C. Sorrell, Ceram. Int. 39 (2013) 3129–3134.
[56] F. Chen, X. Shen, Y. Wang, J. Zhang, Appl. Catal. B: Environ. 121–122 (2012) 223–229.
[57] L. Zhang, Q. Zhang, H. Xie, J. Guo, H. Lyu, Y. Li, Z. Sun, H. Wang, Z. Guo, Appl. Catal. B: Environ. 201 (2017) 470–478.